JGR Space Physics

RESEARCH ARTICLE
10.1029/2025JA034176

Electrostatic Thermal Noise in Magnetized Weakly Ionized Collisional Plasmas

Xianming Zheng[1,2,3], Mihailo M. Martinović[4], Kristopher G. Klein[4], Viviane Pierrard[5,6], Mingzhe Liu[7], Winry Ember[7], Tao Wu[1], Yang Wang[1,2], Jingchun Li[8], Bingkun Yu[1,2], and Xianghui Xue[2]

[1]Deep Space Exploration Laboratory, Institute of Deep Space Sciences, Hefei, China, [2]CAS Key Laboratory of Geospace Environment, Department of Geophysics and Planetary Sciences, University of Science and Technology of China, Hefei, China, [3]LESIA, Observatoire de Paris, Meudon, France, [4]Lunar and Planetary Laboratory, University of Arizona, Tucson, AZ, USA, [5]Royal Belgian Institute for Space Aeronomy (BIRA-IASB), Space Physics, Solar-Terrestrial Center of Excellence, Brussels, Belgium, [6]Earth and Life Institute – Climate Sciences (ELI-C), Université Catholique de Louvain, Louvain-la-Neuve, Belgium, [7]Space Sciences Laboratory, University of California, Berkeley, CA, USA, [8]Shenzhen Key Laboratory of Nuclear and Radiation Safety, Institute for Advanced Study in Nuclear Energy & Safety, College of Physics and Optoelectronic Engineering, Shenzhen University, Shenzhen, China

Key Points:

- We have developed a quasi-thermal noise (QTN) model that accounts for both magnetization and collisions
- The model is developed based on QTN in the Earth's and planetary ionospheres
- The QTN harmonics are influenced by both the magnetic field strength and the orientation angle between the antenna and the magnetic field

Correspondence to:
B. Yu,
bkyu@ustc.edu.cn

Citation:
Zheng, X., Martinović, M. M., Klein, K. G., Pierrard, V., Liu, M., Ember, W., et al. (2026). Electrostatic thermal noise in magnetized weakly ionized collisional plasmas. *Journal of Geophysical Research: Space Physics*, *131*, e2025JA034176. https://doi.org/10.1029/2025JA034176

Received 8 MAY 2025
Accepted 9 DEC 2025

Abstract Quasi-thermal noise (QTN) spectroscopy is a plasma diagnostic technique that enables precise measurements of moments for the local electron velocity distribution function. Previous studies on the QTN technique applied to weakly ionized collisional plasma were limited by the assumptions of unmagnetized and Maxwellian distributions. In this paper, we extend prior research by considering collisional and a secondary hot Maxwellian distribution. Further analysis indicates that as the collision frequency increases, the peak power spectral density at the electron plasma frequency f_p decreases. In addition, we find that the influence of collisions on low-frequency cyclotron harmonic signals in a magnetized plasma is mainly related to the plasma-to-electron cyclotron frequency ratio ω_{pe}/Ω_{ce}, but also has non-trivial dependencies on the plasma Debye Length L_D. Finally, we observed that in eight representative cases, the plasma harmonic disappearance frequency ratio is generally ∼0.25. Our research provides valuable theoretical guidance for the future application of QTN techniques in detecting plasma parameters, especially for collision frequencies typical of Earth's ionosphere.

Plain Language Summary Quasi-thermal noise techniques are particularly effective for plasma diagnostics using electric field antennas onboard space missions. The noise appears as a voltage power spectrum, from which key plasma parameters—such as electron density, temperature, and magnetic field properties—can be inferred. Existing applications of QTN analysis primarily rely on theoretical models developed for solar wind conditions, where the influences of background magnetic fields and plasma collisions are typically neglected. However, such simplifications are not applicable in the context of the Earth's or planetary ionospheres. To address this, we propose a QTN model suitable for ionospheric observations, building upon previous work. This model includes the effects of background magnetic fields and plasma collisions, making it a more comprehensive tool for studying ionospheric plasma.

1. Introduction

A passive electric field antenna connected to a sensitive wave receiver and immersed in a plasma provides a precise method for in situ measurement of the quasi-thermal noise (QTN) spectrum, which originates from the random thermal motions of electrons and ions (Meyer-Vernet, 1979; Meyer-Vernet & Perche, 1989). The QTN spectrum is determined entirely by the plasma velocity distribution function (VDF) and the characteristics of the antenna coupling to ambient electric field fluctuations. When the electron velocity distribution is isotropic and the magnetic field can be neglected (i.e., the electron cyclotron frequency is much smaller than the plasma frequency f_p), the measurement becomes independent of antenna orientation (Martinović et al., 2022; Meyer-Vernet & Perche, 1989). The QTN spectrum exhibits three characteristic regions (Martinović, 2016; Martinović et al., 2020; Meyer-Vernet et al., 2017): (a) a thermal plateau at frequencies $f < f_p$, scaling with the square root of the electron core temperature (Liu, 2022), (b) a sharp plasma resonance peak just above f_p, and (c) a high-frequency branch scaling with the total plasma pressure. From these features, independent estimates of

© 2025. American Geophysical Union. All Rights Reserved.

electron density n_e (Bale et al., 2008), core temperature T_c, and effective kinetic temperature T_e (Liu et al., 2023; Maksimovic et al., 2020; Martinović, 2016) can be extracted.

This diagnostic technique has been widely applied to in situ plasma studies across diverse space environments. In the solar wind, QTN measurements have provided accurate determinations of density, temperature, and suprathermal electron populations (Hoang et al., 1980; Issautier et al., 1999; Issautier et al., 1996; Le Chat et al., 2011; Liu et al., 2023; Maksimovic et al., 1998; Martinović, 2016; Martinović et al., 2020). In planetary magnetospheres, QTN has revealed the structure of cold electron populations, trapped particle distributions, and large-scale density variations, as demonstrated in studies of Jupiter and Saturn (Dazzi et al., 2025; Meyer-Vernet et al., 1993; Moncuquet et al., 2005; Moncuquet et al., 1995; Zheng et al., 2025). QTN has been applied in planetary ionospheres to study density irregularities and temperature effects in observations and simulations (Collinson, Glocer, et al., 2022; Collinson, Ramstad, et al., 2022; Maj & Cairns, 2017; Martinović et al., 2017; Tannous et al., 2024; Zabotin et al., 2001).

These observations in the solar wind have revealed the importance of suprathermal electron populations in governing space plasma processes. In weakly collisional regimes, the Maxwellian description is insufficient, and multi-component VDFs—such as two-Maxwellians or kappa models—are required to capture both the core and halo contributions (Couturier et al., 1981; Le Chat et al., 2010; Martinović et al., 2022; Zheng et al., 2024). The plasma peak and high-frequency wing of the QTN spectrum are especially sensitive to variations in the density and temperature of the secondary, higher-energy populations, making QTN a unique diagnostic of non-equilibrium electron populations and heliosphere energy transport (Liu et al., 2021; Martinović et al., 2020; Zheng et al., 2024).

QTN also offers a powerful diagnostic of electron parameters for magnetospheric plasmas; early investigations established its role in constraining density and temperature distributions at Jupiter and Saturn (Meyer-Vernet et al., 1993; Moncuquet et al., 2005). More recent kinetic models incorporating magnetization show that collisions and wave damping imprint measurable features on the spectrum, providing valuable insights into energy dissipation in magnetized plasma (Dazzi et al., 2025; Zheng et al., 2025). These advances highlight QTN as a probe not only of thermodynamic parameters but also of transport and energization processes in magnetospheres.

In ionospheric plasmas, foundational work by Meyer-Vernet (Meyer & Vernet, 1974) derived expressions for antenna impedance, which were later refined and validated against data (Meyer-Vernet, 1978; Meyer & Vernet, 1975). However, ionospheric plasmas—particularly at lower altitudes—are dominated by frequent electron-neutral collisions that significantly modify antenna impedance and the resulting noise spectra (Balmain, 1964). Early rocket measurements highlighted the importance of collisional damping (Hoang, 1972), while subsequent laboratory experiments validated hydrodynamic descriptions as an approximate solution (Blackwell et al., 2007). More recent work has revealed the limitations of fluid-based models and emphasized the need for kinetic approaches that account for non-Maxwellian VDFs, magnetization, and altitude-dependent collisionality (Dazzi et al., 2025; Martinović et al., 2017). These refinements are critical for capturing conditions in all layers of the ionosphere, where partial ionization and weak magnetization are strongly shaped (Cnossen et al., 2024).

In the Earth's ionosphere above the D layer, previous investigations of collisional QTN under ionospheric conditions (Martinović et al., 2017) were limited to Maxwellian distributions and neglected magnetization effects, thereby not accurately capturing the plasma environment. To address this limitation, the present work extends the analysis by incorporating both Maxwellian velocity distribution functions (VDFs) and two-Maxwellian distributions, while explicitly accounting for magnetization. This comprehensive model seeks to capture the complexity of weakly collisional QTN in the ionosphere and to more realistically represent partially ionized plasma environments.

This paper is organized as follows: Section 2 presents the antenna orientation and response function for magnetized plasmas, along with the expressions of the QTN spectrum for both single- and two-Maxwellian distributions. Section 3 discusses the results of the electric field power spectrum for collisional plasma (excluding antenna effects), the corresponding QTN spectra, and the key factors influencing collisional plasma QTN. Finally, Section 4 summarizes the principal characteristics of collisional plasma and highlights potential avenues for future applications.

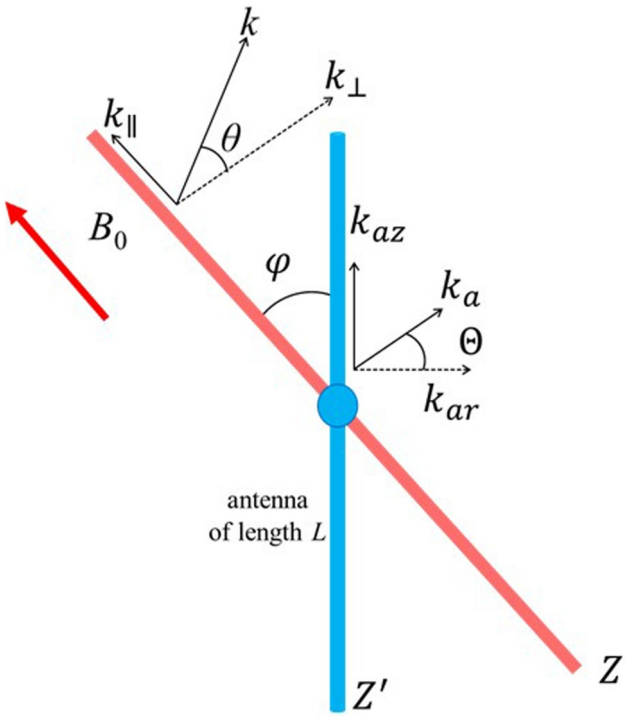


Figure 1. Schematic representation of the wire dipole antenna geometry, illustrating the orientation of the antenna arms and the reference coordinate systems employed as the basis for the analytical and numerical formulations in this work.

2. Methodology

2.1. Antenna Orientation and Response Function

2.1.1. Antenna Orientation and Field Geometry Relative to Wave Vectors and Ambient Magnetic Field

In Figure 1, we illustrate the geometry under consideration in this work. The blue line represents the electric field antenna, and the red line indicates the background magnetic field direction. Here, $k_{\parallel}$ and $k_{\perp}$ denote the parallel and perpendicular components of the wave vector k, with the parallel component aligned with the magnetic field. The angle θ is defined as the azimuthal angle of k in a cylindrical coordinate system where the magnetic field direction is taken as the z-axis (Dazzi et al., 2025). Similarly, k_a, $k_{\rm az}$, and $k_{\rm ar}$ represent the wave vector direction in the antenna-based reference frame, as well as its parallel and perpendicular components in that frame. In addition, Θ denotes the azimuthal angle of the wave vector in the antenna reference frame, and φ denotes the angle between the antenna and the magnetic field.

In this work, we make some assumptions about some parameters. In particular, the antenna has a length $L \ll \lambda$ and a radius $a \ll [\lambda_D, L]$, and we assume $f_{\rm pe}/f_{\rm ce} > 1$, where $f_{\rm pe} = \frac{1}{2\pi}\sqrt{\frac{n_e e^2}{\varepsilon_0 m_e}}$ is the plasma oscillation frequency and $f_{\rm ce} = qB/2\pi m_e$ is the electron gyrofrequency. Here, a and λ are the antenna radius and the wavelength, respectively, $\lambda_D = \sqrt{\frac{\varepsilon_0 k_B T_e}{n_e e^2}}$ is the Debye length, ε_0 is the vacuum permittivity, n_e is the electron density, T_e is the electron temperature, and B is the background magnetic field. The subsequent discussion is based on and satisfies these assumptions. Based on the above assumptions and previous theories, we can obtain (Meyer-Vernet et al., 2017):

$$V^2 = \frac{8}{\pi^2}\int_0^{\infty} \mathrm{dk}\, F(\mathrm{kL}) \left\langle E^2(k,\omega)\right\rangle \tag{1}$$

In Equation 1, $F(\mathrm{kL})$ is the antenna response function, and $E(k,\omega)$ represents the electric field fluctuations; in the following, I will analyze these two components separately.

2.1.2. The Antenna Response Function in Magnetized Plasma

For the simplest antenna, comprising two aligned wires without a gap between the arms, the response function in a magnetized plasma is detailed in Appendix A (Dazzi et al., 2025).

$$F(k,L) = \frac{1}{32\pi}\int_0^{2\pi} \left| \frac{4}{Lk_z^2} J_0(k_r a) \sin^2\left(\frac{k_z L}{2}\right) \hat{z}\cdot\vec{k} \right|^2 d\theta \tag{2}$$

where,

$$k_{\rm az} = \hat{z}\cdot\vec{k} = k_{\perp}\cos\theta\sin\varphi + k_{\parallel}\cos\varphi \tag{3}$$

$$k_{\rm ar} = \sqrt{k_{\perp}^2\cos^2\theta\cos^2\varphi + k_{\parallel}^2\sin^2\varphi - 2k_{\perp}k_{\parallel}\cos\theta\cos\varphi\sin\varphi + k_{\perp}^2\sin^2\theta} \tag{4}$$

Here, a represents the antenna radius, θ represents the angle in cylindrical coordinates around the magnetic field, $k_{\parallel}$ and $k_{\perp}$ denote the wave vector components parallel and perpendicular to the background magnetic field, respectively, and J is the Bessel function. Additionally, φ is the angle between the antenna and the ambient constant magnetic field.

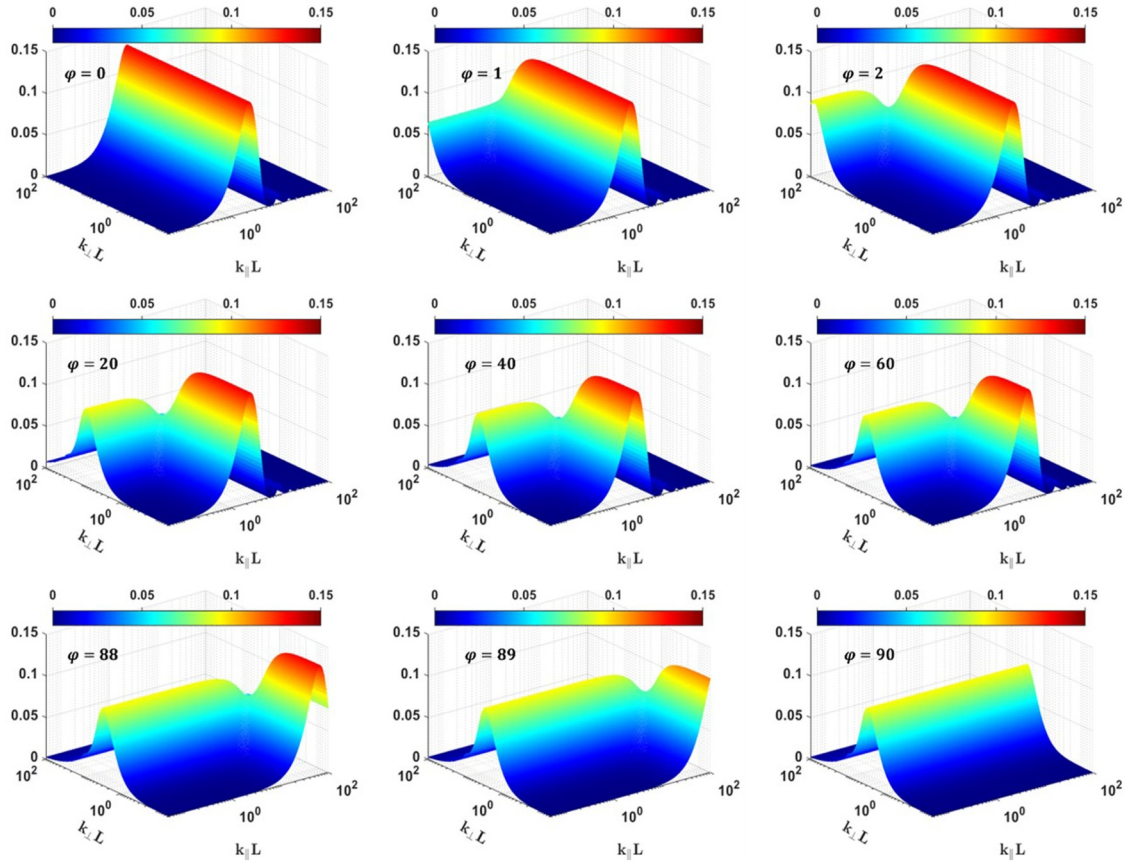


Figure 2. The reduced antenna response function in magnetized plasma for wire dipole antenna Equation 2. The x-axis represents $k_{\parallel} L$, the y-axis presents $k_{\perp}L$, and the z-axis and color scale represent the intensity of the antenna response function.

In Figure 2, we present the reduced antenna response function defined in Equation 2 in the $(k_{\parallel}, k_{\perp}, \theta)$ space for different φ angles. The results show that when φ is relatively small <10° and particularly when the angle is 0, there is a peak at $(k_{\parallel} L \approx 1)$. When $(\varphi > 0°)$, another peak appears at $k_{\perp} L$, and the position of this peak gradually decreases along $k_{\perp} L$ as φ increases. When $(\varphi = 90°)$, there is only one peak at $(k_{\perp} L \approx 1)$, and this peak is smaller than the corresponding peak at $(\varphi = 0°)$. That means that when $\varphi = 0$, the electric field antenna has different responses to signals in the parallel direction for different wavelengths, whereas for signals in the perpendicular direction, the response is the same for all wavelengths. Conversely, when $\varphi = 90$, the situation is reversed compared to when $\varphi = 0$.

2.2. Plasma Dielectric Response and Quasi-Thermal Noise Signal

2.2.1. Quasi-Thermal Noise in Single-Maxwellian Magnetized Collisional Plasms

For plasma in thermal equilibrium, the longitudinal electric fluctuations are described as follows:

$$\left\langle E^2\,(k,\omega)\right\rangle = \frac{\left\langle \rho^2(k,\omega)\right\rangle^{(0)}}{k^2\epsilon_0^2|\epsilon_L(k,\omega)|^2} \tag{5}$$

where $\epsilon_L(k,\omega)$ and $\rho(k,\omega)$ are longitudinal dielectric function and the free space (test particle) charge density fluctuations. $\rho(k,\omega)$ is related the plasma density, and $\epsilon_L(k,\omega)$ can be obtained for collisional, weakly ionized plasma using the Vlasov equation, and the collision term is given by Bhatnagar et al. (Bhatnagar et al., 1954). Assuming a Maxwellian particle VDF, the dielectric function can be written as follows:

$$\epsilon(\omega,k) = 1 + \frac{1}{k^2 L_D^2}\frac{1 + (z + i\nu')Z_0(\zeta)}{1 + i\nu' Z_0(\zeta)} \tag{6}$$

Here, we use the substitutions $\zeta = z + i\nu'$, $z = \omega/kv_{\rm th}$, $\nu' = \nu/kv_{\rm th}$, where $Z_0(\zeta)$ is the plasma dispersion function (Fried & Conte, 2015), $v_{\rm th} = \sqrt{2k_B T_e/m_e}$ is the electron thermal velocity, and L_D is the Debye length.

In natural space plasmas, the interplay of plasma collisions and magnetic field effects varies depending on the environment (Dubinin et al., 2014; Luhmann & Cravens, 1991). In the solar wind, where plasma density and magnetic field strength are low, collisions are typically negligible, and magnetic field effects remain insignificant. Within planetary magnetospheres, plasma collisions remain insignificant, but magnetic field effects play a critical role. However, in Earth's ionosphere, the ionization of neutral particles leads to a higher density of charged particles, enabling the coexistence of both significant plasma collisions and magnetic field effects. This unique environment makes it particularly important to study the combined influence of these factors. In general, the "longitudinal" dielectric permittivity of nondegenerate weakly ionized plasma is expressed as follows (Alexandrov et al., 1984):

$$\epsilon(\omega,k) = \frac{k_i k_j}{k^2}\epsilon_{ij}(\omega,k) = 1 + \sum_a \frac{\omega_{\rm pa}^2}{k^2 v_{\rm Ta}^2}\frac{1 - \sum_n \dfrac{\omega + i\nu_{\rm an}}{\omega + i\nu_{\rm an} - n\Omega_a} A_n(Z_a) I_+(\beta_{\rm an})}{1 - \sum_n \dfrac{i\nu_{\rm an}}{\omega + i\nu_{\rm an} - n\Omega_a} A_n(Z_a) I_+(\beta_{\rm an})}. \tag{7}$$

Where $Z_a = k_\perp^2 v_{\rm Ta}^2/\Omega_a^2$, $\beta_{\rm an} = (\omega + i\nu_{\rm an} - n\Omega_a)/k_z v_{\rm Ta}$, $A_n(Z_a) = e^{-Z_a} I(Z_a)$, $I_+(\beta_{\rm an}) = -\beta_{\rm an} * Z(\beta_{\rm an})$, $\Omega_a = qB/m_a$, q represents the electric charge, and B is the background magnetic field. Here, $\nu_{\rm an}$ represents the collision frequency, I is the modified Bessel function, and Z is the plasma dispersion function.

2.2.2. Two Maxwellians in Magnetized and Weakly Ionized Collisional Plasmas

For the two-Maxwellian distribution, we will also consider the suprathermal electron component to calculate the plasma dispersion function. The expression for the dielectric tensor of the two-Maxwellian distribution, considering collisional effects, can be extended from Equation 4 as follows (Dazzi et al., 2025):

$$\begin{aligned}\varepsilon_L(k_\perp, k_\parallel, \omega) = 1 + \frac{1}{k_N^2}\frac{\left(\dfrac{1 + \omega_N + i\nu_{c,N}\sum_{-\infty}^{+\infty} I_n(\lambda_c)\, e^{-\lambda_c} Z_0\left(\zeta_n^{\nu,c}\right)}{\sqrt{2}\, k_{\parallel,N}}\right)}{\left(\dfrac{1 + i\nu_{c,N}\sum_{-\infty}^{+\infty} I_n(\lambda_c)\, e^{-\lambda_c} Z_0\left(\zeta_n^{\nu,c}\right)}{\sqrt{2}\, k_{\parallel,N}}\right)} + \\ \frac{1}{k_N^2}\frac{\alpha}{\tau}\frac{\left(\dfrac{1 + \omega_N + i\nu_{h,N}\sum_{-\infty}^{+\infty} I_n(\lambda_h)\, e^{-\lambda_h} Z_0\left(\zeta_n^{\nu,h}\right)}{\sqrt{2}\, k_{\parallel,N}}\right)}{\left(\dfrac{1 + i\nu_{h,N}\sum_{-\infty}^{+\infty} I_n(\lambda_h)\, e^{-\lambda_h} Z_0\left(\zeta_n^{\nu,h}\right)}{\sqrt{2}\, k_{\parallel,N}}\right)}\end{aligned} \tag{8}$$

$$\lambda_c = k_\perp^2 \lambda_D * \frac{\omega_{pe,c}^2}{\Omega_{\rm ce}}\zeta_n^{\nu,c} = \frac{\omega + {\rm i}\nu - n\Omega_{ce}}{\sqrt{2}k_\parallel \lambda_D \omega_{{\rm pe},c}}$$

$$\lambda_h = k_\perp^2 \lambda_D * \frac{\omega_{{\rm pe},h}^2}{\Omega_{\rm ce}}\zeta_n^{\nu,h} = \frac{\omega + {\rm i}\nu - n\Omega_{\rm ce}}{\sqrt{2}k_\parallel \lambda_D \omega_{{\rm pe},c}}\frac{1}{\sqrt{\tau}}.$$

In the solar wind plasma, it is generally valid that $\Omega_{ce} \ll \omega_{\mathrm{pe}}$ and $\nu \ll \omega_{\mathrm{pe}}$, so these two terms can usually be neglected. The normalized parameters are as follows:

$$k_N = \sqrt{k_{\parallel}^2 + k_{\perp}^2} * \lambda_D, \qquad \lambda_D = \sqrt{\frac{\epsilon_0 k_B T_e}{n_e q_e^2}}, \qquad \omega_N = \frac{\omega}{\omega_{\mathrm{pe}}}. \tag{9}$$

Where $\alpha = \frac{n_h}{n_c}$, $\tau = \frac{T_h}{T_c}$, and subscripts h and c present the suprathermal (halo) and thermal (core) electrons. The susceptibilities of the core and halo components are additive. The resulting total dielectric tensor under the two-Maxwellian distribution is a function of ε_L ($k_{\parallel}$, $k_{\perp}$, ω, ν, α, τ, n_e, B, T_e).

In Section 2.1, we present the expression for the antenna response function. However, QTN is determined not only by the antenna response function but also by electrostatic field fluctuations. The electrostatic field fluctuation signal is independent of the antenna and primarily depends on the distribution function of the space plasma. Its main expression is as follows (Yoon et al., 2017):

$$(2\pi)^4 \langle \delta E^2 \rangle_{k,\omega} = \frac{8\pi T}{\omega} \frac{\mathrm{Im}\epsilon(k,\omega)}{|\epsilon(k,\omega)|^2}, \tag{10}$$

$$S(k,\theta,\omega) = \frac{2\pi^3 \omega_p}{T} \langle \delta E^2 \rangle_{k,\omega}. \tag{11}$$

If the electrostatic field fluctuations are isotropic in the antenna frame and the antenna response function is taken into account, the QTN can be expressed as follows:

$$V_f^2 = \frac{16 m_e v_{\mathrm{th}} L_D}{\pi \epsilon_0} \iint_0^{\infty} \frac{F(k_{\perp}, k_{\parallel}) * \mathrm{Im}\epsilon_L(k_{\perp}, k_{\parallel}\omega)}{\pi \omega_N |\epsilon_L(k_{\perp}, k_{\parallel}\omega)|^2} dk_{\perp} dk_{\parallel}. \tag{12}$$

3. Results and Discussion

3.1. The Collisional Plasma QTN Generic Spectrum

First, we discuss the results for the case of single-Maxwellian distribution. The results are displayed in Figure 3. It presents the plasma oscillation results when the angle between the antenna and the magnetic field is $\varphi = 60$. (In Figure 5, we calculate that the QTN exhibits a relatively significant harmonic signal only when $\varphi \geq 60$). The results show that when the magnetic field and plasma collisions are introduced, significant changes occur in the low frequency ($f < f_{\mathrm{pe}}$) and $f \approx f_{\mathrm{pe}}$ regions of the QTN. At low frequencies, signal enhancing, and at $f \approx f_{\mathrm{pe}}$ signal attenuation is observed and broadening (measured by the full width at half maximum of the QTN peak) occurs. f_p regions of the oscillations quickly dissipate energy, resulting in a stronger signal in the $f < f_{\mathrm{pe}}$ region. As the collision frequency increases, the damping effect of the plasma on f_{pe} oscillations becomes more pronounced, leading to the attenuation of f_{pe} components and a relative increase in the low-frequency signal. Additionally, at $f > f_{\mathrm{pe}}$, the power spectrum remains unchanged because the $f > f_{\mathrm{pe}}$ frequency part is simply a reflection of the total pressure, which does not vary. In general, collisions lead to spectral broadening (Jorge et al., 2019), as more frequent particle interactions increase the line width and reduce the signal strength in certain frequency bands, which can hinder precise measurements of plasma parameters. Collisions also reduce the amplitude of high-frequency components by limiting electron free motion, leading to a flattening effect on the QTN spectrum and impacting parameter extraction, such as electron temperature. For core electron temperature, collisions introduce additional noise and spectral distortion, potentially causing overestimation when using conventional QTN-based methods.

For the Maxwellian distribution, the results of the electrostatic fluctuations show that collisions act as a damping effect. This means that as the collision frequency increases, the amplitude of the plasma peak decreases. Moreover, this effect is not limited to the peak but also influences the low-frequency electron Bernstein wave region of the spectrum. Specifically, when strong electron-neutral atom collisions occur, the electron Bernstein waves are suppressed.

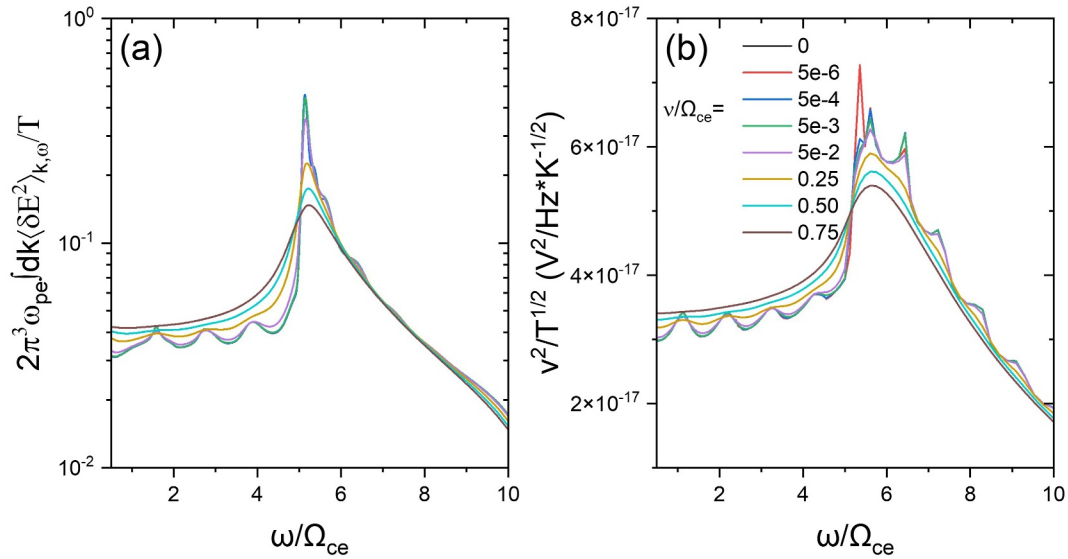


Figure 3. Left panel (a): Results of the electric field fluctuations calculated using the Maxwellian distribution for different collision frequencies (without considering the influence of the antenna). Right panel (b): The electron quasi-thermal noise (QTN) results are based on the Maxwellian distribution with the antenna response function at $\varphi = 60$. The legend in the figure represents the collision frequency, which is the same as in panel (a). The results show that when the collision frequency exceeds $\nu/\Omega_{ce} \sim 0.25$, the QTN harmonic structure disappears.

Figure 4 shows the electric field power spectrum and QTN results for the two-Maxwellian distribution. The two-Maxwellian calculations show that, as the suprathermal electron temperature τ increases, the QTN peak increases (Couturier et al., 1981). Moreover, when considering electron-neutral atom collisions, this result is consistent with the calculation results of the single Maxwellian. That is, plasma collisions can influence the peak power spectrum of the QTN, and as collisions increase, they lead to the suppression of electron Bernstein waves in magnetized plasma. It is therefore important to emphasize that while higher τ enhances the QTN peak, the collision frequency (ν) counteracts this effect by lowering the spectral intensity. Such competing influences may introduce biases in the estimation of τ and ν when fitting ionospheric plasma parameters using a two-Maxwellian model.

A representative example arises in the transition region between the D and E layers in the Earth's ionosphere, between altitudes of ~90–120 km. In this region, the ambient magnetic field is approximately $(3 - 5) \times 10^{-5}\ T$, corresponding to electron gyrofrequencies in the kHz–MHz range. At the same time, the electron–neutral collision frequency has been reported to lie within $10^3 - 10^5 s^{-1}$, corresponding to $\nu/\omega_{pe} \sim 10^{-2} - 10^{-1}$ (Benson, 1964; Pandey & Vladimirov, 2018; Sarkar et al., 2025; Spencer et al., 2008). Table 1 presents the typical ranges of parameters in the ionospheres of Earth, Venus, and Mars, including electron density, temperature, Debye length, collision frequency, and electric field fluctuation.

Furthermore, the simulation results in Figures 3b and 3d, when $\alpha = 10^{-3}$ and $\tau = 20$, as the collision frequency ν/Ω_{ce} increases from 5×10^{-3} to 5×10^{-2}, both the electric fluctuations and the QTN power spectrum decrease significantly. At $\nu/\Omega_{ce} = 5 \times 10^{-2}$, the suprathermal contribution of the two-Maxwellian distribution is almost entirely suppressed, yielding results that closely resemble those of the single-Maxwellian case. In Appendix A, we also provide a vertical profile of the collisional probability versus the QTN spectrum peak shift with ionospheric height.

3.2. The Impact of Collisions to Electric Fluctuations and QTN

3.2.1. The Impact of Collision Effects in $f < f_p$

In Figures 2 and 3, we observe that when $\nu/\Omega_{ce} \approx 0.25$, the Bernstein harmonics in the electric field fluctuations and QTN disappear. Using the Maxwellian distribution function as an example, we calculate the electric field fluctuations. Additionally, we investigate the effects of ω_{pe}/Ω_{ce} and the Debye length (L_D) on low-frequency electric field fluctuations in collisional plasmas.

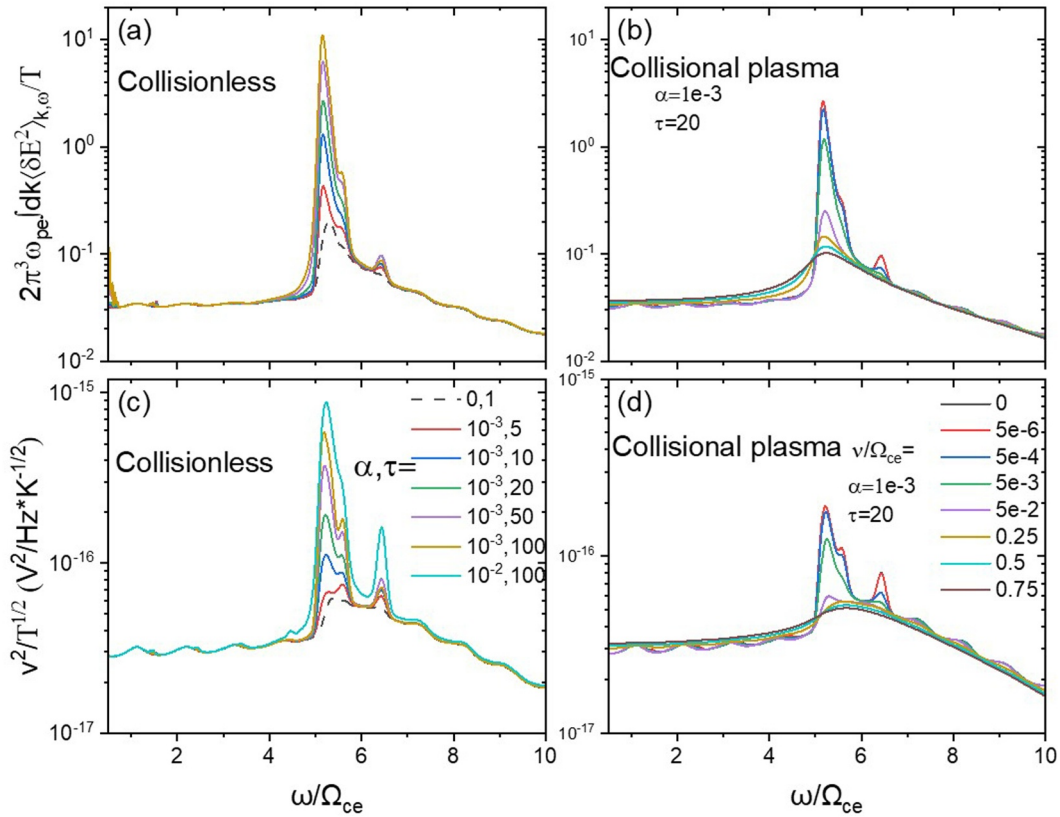


Figure 4. Results of the electric field fluctuations based on the two-Maxwellian electron distribution and quasi-thermal noise (QTN). Panels (a, b) show the electric field fluctuation results, while panels (c, d) show the QTN results. Similar to Figure 3, the antenna response function also comes from the 2D antenna response function. The results still show that when $\frac{\nu}{\Omega_{ce}} \approx 0.25$, the Bernstein waves disappear, which is consistent with the Maxwellian results. In these results, we have set $\nu_h = \nu_c$.

In Figure 5, we present the relationship between plasma electric field fluctuations and the ratio of plasma frequency to electron cyclotron frequency. In this theoretical calculation, we set $\omega_{pe} = 1.93 \times 10^6$ rad/s and $V_{th} = 1.23 \times 10^5$ m/s in Figure 5e. Subsequently, in Figures 5f, 5g, and 5h, the thermal velocity is set to $2V_{th}$, $3V_{th}$, and $4V_{th}$, respectively. The results show that as this ratio increases, the electric field fluctuation signal

Table 1
Typical Ranges of Key Plasma Parameters in the Ionospheres of Earth, Venus, and Mars (90 ~ 300 km): Electron Density, Temperature, Debye Length, Collision Frequency, and Electric Field Fluctuations

Parameters	Symbol	Venus/Reference	Earth/Reference	Mars/Reference
Electron density (m^{-3})	N_e	$(0.01 \sim 1.6) \times 10^{10}$ Shinagawa (1996); Miller et al. (1980); Russell and Vaisberg (1983)	$(1 \sim 1.5) \times 10^{11}$ Gurevich and Budden (1980); Kelley (2009)	$(0.1 \sim 60) \times 10^{10}$ Withers et al. (2008)
Electron temperature (K)	T_e	$(2 \sim 30) \times 10^2$ Cravens et al. (1980); Miller et al. (1980)	200 ~ 500 Kelley (2009); Gurevich and Budden (1980)	$(2 \sim 4) \times 10^2$ Choi et al. (1998)
Debye length (m)	λ_D	$(7.7 \sim 30) \times 10^{-3}$ Miller et al. (1980)	$(2.5 \sim 4.9) \times 10^{-3}$ Gurevich and Budden (1980); Kelley (2009)	$(6.5 \sim 26) \times 10^{-3}$ Withers et al. (2008)
Collision/plasma oscillation	ν/ω_{pe}	$(0.008 \sim 2.4) \times 10^{-3}$ Dubinin et al. (2014)	$(0.2 \sim 8.1) \times 10^{-3}$ Sarkar et al. (2025)	$(0.5 \sim 6) \times 10^{-3}$ Peter et al. (2024)
Ambipolar electric field (V/m)	$E_{Ambipole}$	$10^{-6} \sim 10^{-5}$ Collinson et al. (2023)	$\sim 10^{-6}$ Collinson et al. (2024)	$\sim 10^{-6}$ Akbari et al. (2019)
Electric field fluctuation (V/m)	$E_{fluctuation}$	$(0.1 \sim 1) \times 10^{-3}$ Russell et al. (2013)	$(1 \sim 10) \times 10^{-3}$ Kelley (2009)	$(0.08 \sim 5) \times 10^{-3}$ Fowler et al. (2017)

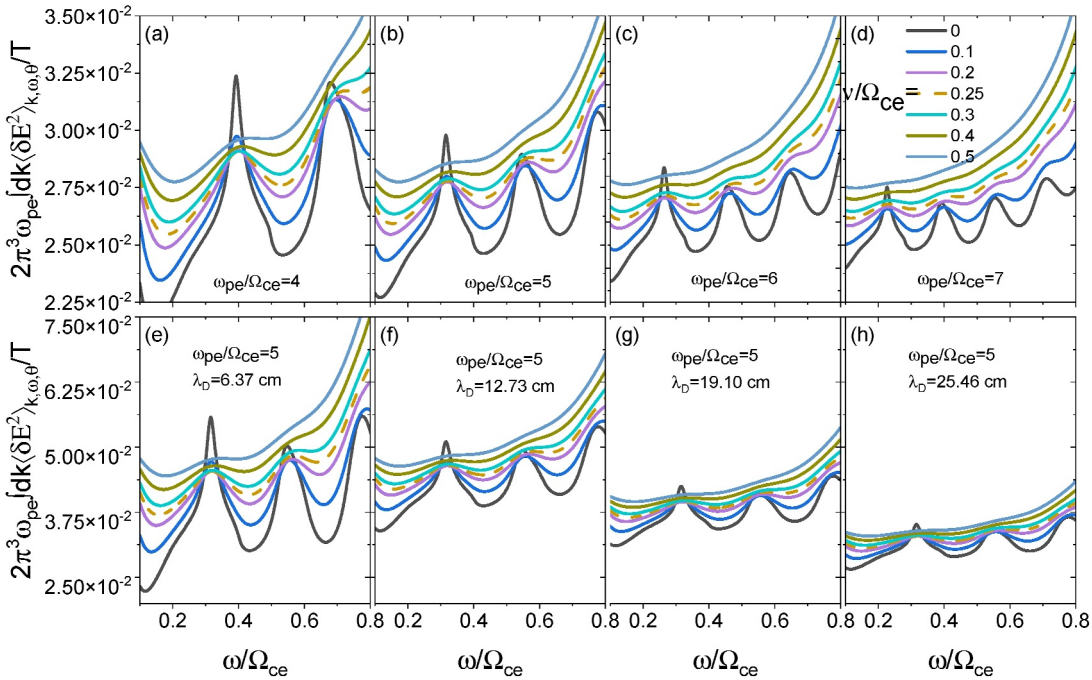


Figure 5. Electric field fluctuations vary with parameters. Panels (a–d) show the results of plasma electric field fluctuations varying with ω_{pe}/Ω_{ce}, while Figures (e–h) illustrate the variation of plasma electric field fluctuations with the Debye length λ_D. We set $\omega_{pe} = 1.93 \times 10^6$ rad/s and $V_{th} = 1.23 \times 10^5$ m/s in figure (e), in Figures 4f–4h, within the same theoretical model, only the thermal velocity is varied.

becomes smoother, and the harmonics are not prominent at low frequencies, and in all collision cases, the signal becomes more concentrated. Additionally, there is a slight overall downward trend in the signal. For smaller ratios, the collision frequency at which the Bernstein harmonic corresponding to the harmonics disappears is higher.

According to the results in panels (e) to (h), similar to panels (a) to (d), when the Debye length increases, the signal becomes more monochromatic. The difference in the signal becomes smaller in all collision frequency cases. Moreover, there is an overall downward trend in the signal as the Debye length increases from low to high values. Additionally, as in the previous analysis, for low Debye lengths, the collision frequency at which the corresponding harmonics of the Bernstein harmonic disappear is higher, while for high Debye lengths, the collision frequency at which the corresponding harmonics disappear is lower. We have only discussed the case where $\omega < \omega_p$, as the collision effects are not significant when $\omega > \omega_p$, and thus this case has not been considered.

3.2.1.1. How Does the Antenna Angle Affect QTN?

Figure 6 illustrates the influence of the 2D antenna response function on the QTN results. Panels (a) and (b) represent the electric field fluctuations without considering the antenna for single Maxwellian and two-Maxwellian, respectively. In this signal, distinct harmonic features can be observed. Panel (c) shows the QTN signal for the single Maxwellian case. In this signal, distinct harmonic features can be observed. Panel (d) displays the QTN signal for the two-Maxwellian case, with the corresponding numbers indicating the angle φ between the antenna and the background magnetic field. The results show that when φ is less than 10°, the QTN signal contains almost no harmonic signals. As the angle increases from 10° to 60°, the QTN harmonics become more pronounced. When the angle φ exceeds 60°, the QTN signal remains essentially constant. This result suggests that the variation in the angle between the antenna and the magnetic field leads to the phenomenon of Bernstein waves, which has also been observed in previous studies (Meyer-Vernet et al., 1993). Therefore, when using electric field antennas to measure magnetized plasmas, the cyclotron harmonics will be captured only when the angle between the antenna and the magnetic field is greater than 60°.

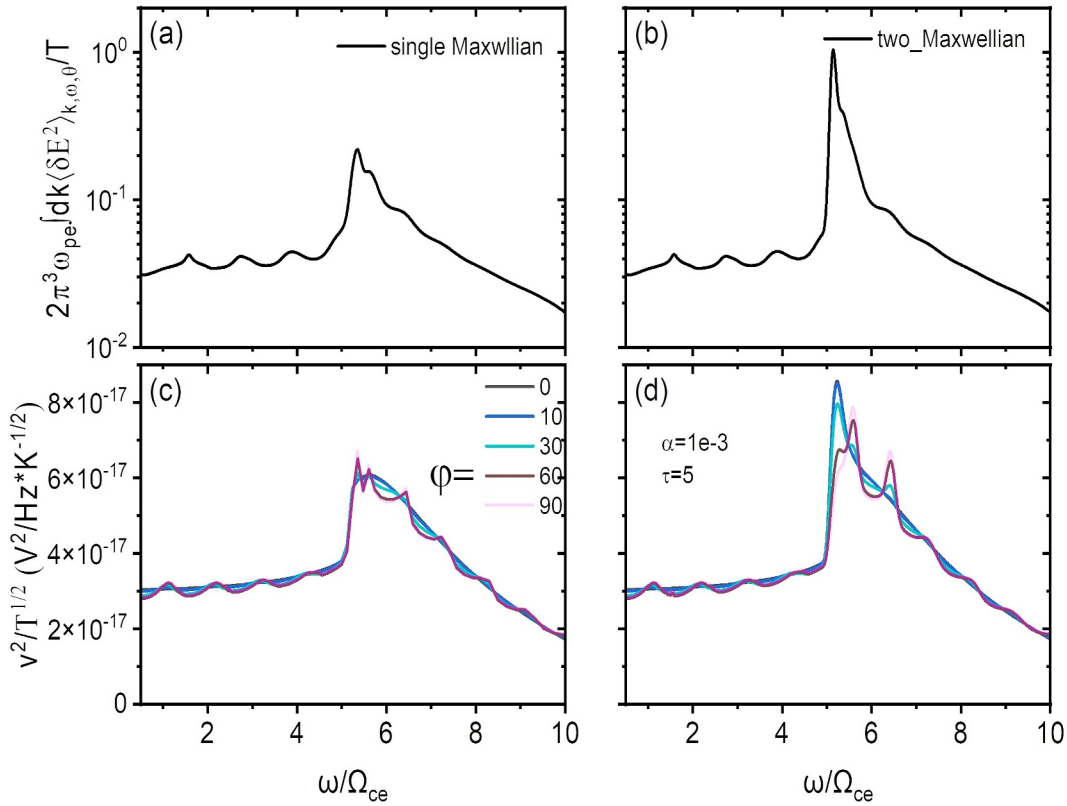


Figure 6. The effect of the angle φ (0°, 10°, 30°, 60°, 90°) between the antenna and the magnetic field on quasi-thermal noise (QTN), with $\frac{\omega_{pe}}{\Omega_{ce}} = 5$. Top panels: without considering the antenna. Bottom panels: QTN signal. Left panels: Single Maxwellian case. Right panel: Two-Maxwellian case. Panels (a) and (c) show the electric field fluctuations derived assuming a Maxwellian electron distribution, and the corresponding QTN power spectra for different angles between the antenna and the magnetic field, respectively. Panels (b) and (d) present the electric field fluctuations based on a two-Maxwellian electron distribution, together with the resulting QTN power spectral densities for different antenna–magnetic field orientations.

4. Conclusions

In this paper, we developed a QTN model for collisional plasmas, building upon previous theoretical frameworks. We first introduced a two-dimensional antenna response function model, analyzed its behavior under varying φ conditions, and incorporated it into QTN calculations. By examining single-Maxwellian and two-Maxwellian distributions under collisional effects, we found that increasing collision frequency leads to a slight enhancement of power spectral density for $f < f_p$, while reducing it around $f \approx f_p$, with minimal impact at $f > f_p$. Furthermore, when $\nu/\Omega_{ce} > 0.25$, Bernstein harmonics and superthermal effects in the low-frequency QTN spectrum vanish.

We further examined three key factors influencing low-frequency electric field fluctuations in collisional plasmas: ω_{pe}/Ω_{ce}, Debye length L_D, and the antenna-magnetic field angle φ. Our results indicate that higher ω_{pe}/Ω_{ce} or larger L_D suppress collision-induced effects, thereby reducing fluctuation intensity. This indicates that stronger electromagnetic characteristics in the plasma enhance the amplitude and intensity of electric field fluctuations, whereas electrostatic properties and collisions tend to suppress them. In particular, when the collision frequency is high, the contribution of suprathermal electrons and the generation of Bernstein harmonics are inhibited. Distinct Bernstein harmonic signals appear in magnetized plasmas when $\varphi > 60°$.

The proposed model offers a robust foundation for future studies of planetary ionospheres, particularly for plasma parameter inversion in Earth's ionosphere. Recent advances in QTN analysis have demonstrated strong potential for diagnosing key plasma parameters in the ionosphere (Maj & Cairns, 2017). Simultaneously, the ongoing development of NASA's Geospace Dynamics Constellation (GDC) has motivated the construction of community observing system simulation experiment tools, which support global ionosphere–thermosphere research and

highlight the importance of multi-parameter observations in data assimilation and forecasting (Hsu et al., 2024; Rowland et al., 2022). The AQTN model for collisional ionospheric plasma can therefore provide abundant observational data in support of GDC measurements, facilitating the refinement and improvement of models of the ionosphere.

While the QTN model captures key collisional and antenna response effects, it assumes homogeneous, stationary plasma and a simplified antenna configuration, omitting turbulence, nonlinearities, and more complex spacecraft antenna geometries. Future work should address these factors to improve applicability to real observational data.

Appendix A: Collision Probability, QTN Peak Shift, and Plasma Parameters in Planetary Ionospheres

To study the variation of the QTN amplitude with altitude in the Earth's ionosphere, we used the International Reference Ionosphere (IRI) model to obtain plasma parameters and the corresponding collision frequency in the 90–600 km altitude range, as shown in Figure A1 (Aggarwal et al., 1979; de Dieu NIBIGIRA & Marchand, 2025). In Figure A1(a), the red line represents the electron density as a function of altitude, and the black line represents the electron temperature. It can be seen that both the electron density and temperature reach local maxima in the

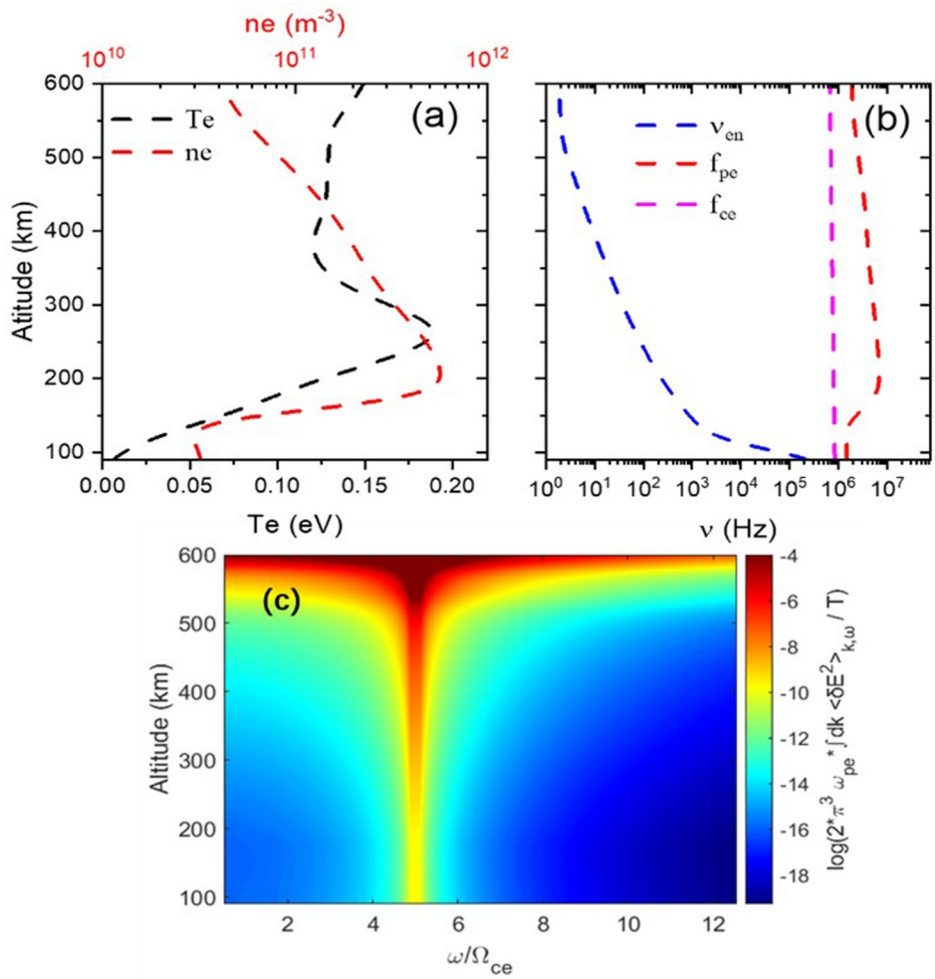


Figure A1. The electron density, temperature, and collision profiles in the 90–600 km altitude range obtained from the Earth's ionospheric IRI model, it is used to compute the quasi-thermal noise (QTN) spectrum peak shift as a function of altitude. (a) Altitude profiles of the electron density and electron temperature in the terrestrial ionosphere derived from the IRI model. (b) Model-derived plasma oscillation frequency f_pe, electron cyclotron frequency f_ce, and plasma–neutral collision frequency ν-en. (c) Altitude–frequency distribution of QTN spectrum peak including the effect of plasma collisions.

150–300 km altitude range. Above this range, the electron density decreases with altitude, while the electron temperature remains approximately constant. Figure A1(b) shows the collision frequency between electrons and neutral atoms, which decreases with altitude, related to the variation of electron density. Figure A1(c) presents the QTN results calculated using the plasma parameters from the model, with $\omega/\Omega_{ce} = 5$ corresponding to the peak frequency. The results indicate that as altitude increases and plasma collisions weaken, the amplitude of the QTN peak increases in 90–600 km.

Conflict of Interest

The authors declare no conflicts of interest relevant to this study.

Data Availability Statement

The IRI model data for the Earth's ionosphere were obtained from the IRI model. The data are publicly available at https://irimodel.org.

The QTN code and the antenna response function code are available at the Zenodo link http://doi.org/10.5281/zenodo.17784575.

Acknowledgments
This work was supported by the National Natural Science Foundation of China (Grants 42188101, 42441808, 42405133, 42474204), the National Natural Science Foundation of China Distinguished Overseas Young Talents Program, Basic Research Project of the National Key Laboratory of Deep Space Exploration (NKLDSE2023A002), and the Frontier Scientific Research Program of Deep Space Exploration Laboratory (2022-QYKYJH-GCXD-004). V.P. acknowledges the project 21GRD02 BIOSPHERE from the European Partnership on Metrology, co-financed by the European Union's Horizon Europe research and innovation program and by the participating states. We thank Dr. Hongyang Zhou (Boston University) for assistance with the code, Karine Issautier and Pietro Dazzi for their guidance on the QTN method, and Naomi Maruyama for insights into ionospheric principles.

References

Aggarwal, K., Nath, N., & Setty, C. (1979). Collision frequency and transport properties of electrons in the ionosphere. *Planetary and Space Science*, *27*(6), 753–768. https://doi.org/10.1016/0032-0633(79)90004-7

Akbari, H., Andersson, L., Peterson, W., Espley, J., Benna, M., & Ergun, R. (2019). Ambipolar electric field in the Martian ionosphere: MAVEN measurements. *Journal of Geophysical Research: Space Physics*, *124*(6), 4518–4524. https://doi.org/10.1029/2018ja026325

Alexandrov, A. F., Bogdankevich, L. S., & Rukhadze, A. A. (1984). *Principles of plasma electrodynamics*. Springer.

Bale, S. D., Ullrich, R., Goetz, K., Alster, N., Cecconi, B., Dekkali, M., et al. (2008). The electric antennas for the STEREO/WAVES experiment, the STEREO Mission (pp. 529–547).

Balmain, K. (1964). The impedance of a short dipole antenna in a magnetoplasma. *IEEE Transactions on Antennas and Propagation*, *12*(5), 605–617. https://doi.org/10.1109/tap.1964.1138278

Benson, R. F. (1964). Electron collision frequency in the ionospheric D region. *J. Res. Natl. Bur. Std.*, *68*.

Bhatnagar, P. L., Gross, E. P., & Krook, M. (1954). A model for collision processes in gases. I. Small amplitude processes in charged and neutral one-component systems. *Physical Review*, *94*(3), 511–525. https://doi.org/10.1103/physrev.94.511

Blackwell, D. D., Walker, D. N., Messer, S. J., & Amatucci, W. E. (2007). Antenna impedance measurements in a magnetized plasma. II. Dipole antenna. *Physics of Plasmas*, *14*(9), 092106. https://doi.org/10.1063/1.2779285

Choi, Y., Kim, J., Min, K., Nagy, A., & Oyama, K. (1998). Effect of the magnetic field on the energetics of Mars ionosphere. *Geophysical Research Letters*, *25*(14), 2753–2756. https://doi.org/10.1029/98gl51839

Cnossen, I., Emmert, J. T., Garcia, R. R., Elias, A. G., Mlynczak, M. G., & Zhang, S.-R. (2024). A review of global long-term changes in the mesosphere, thermosphere and ionosphere: A starting point for inclusion in (semi-) empirical models. *Advances in Space Research*, *74*(11), 5991–6011. https://doi.org/10.1016/j.asr.2024.10.005

Collinson, G., Glocer, A., Pfaff, R., Barjatya, A., Bissett, S., Blix, K., et al. (2022). The endurance rocket Mission: Gauging earth's Ambipolar electric potential. *Space Science Reviews*, *218*(5), 39. https://doi.org/10.1007/s11214-022-00908-0

Collinson, G. A., Frahm, R. A., Glocer, A., Daldorff, L., Thiemann, E., Kang, S. B., et al. (2023). A survey of strong electric potential drops in the ionosphere of Venus. *Geophysical Research Letters*, *50*(18), e2023GL104989. https://doi.org/10.1029/2023gl104989

Collinson, G. A., Glocer, A., Pfaff, R., Barjatya, A., Conway, R., Breneman, A., et al. (2024). Earth's ambipolar electrostatic field and its role in ion escape to space. *Nature*, *632*(8027), 1021–1025. https://doi.org/10.1038/s41586-024-07480-3

Collinson, G. A., Ramstad, R., Frahm, R., Wilson, L., III, Xu, S., Whittlesey, P., et al. (2022). A revised understanding of the structure of the Venusian magnetotail from a high-altitude intercept with a tail ray by Parker Solar Probe. *Geophysical Research Letters*, *49*(1), e2021GL096485. https://doi.org/10.1029/2021gl096485

Couturier, P., Hoang, S., Meyer-Vernet, N., & Steinberg, J.-L. (1981). Quasi-thermal noise in a stable plasma at rest: Theory and observations from ISEE 3. *Journal of Geophysical Research*, *86*(A13), 11127–11138. https://doi.org/10.1029/ja086ia13p11127

Cravens, T., Gombosi, T., Kozyra, J., Nagy, A., Brace, L., & Knudsen, W. (1980). Model calculations of the dayside ionosphere of Venus: Energetics. *Journal of Geophysical Research*, *85*(A13), 7778–7786. https://doi.org/10.1029/ja085ia13p07778

Dazzi, P., Issautier, K., Meyer-Vernet, N., Henri, P., & Martinović, M. (2025). Quasi-thermal noise spectroscopy in magnetized space plasma: Theory and model. *Journal of Geophysical Research: Space Physics*, *130*(3), e2024JA033325. https://doi.org/10.1029/2024ja033325

de Dieu Nibigira, J., & Marchand, R. (2025). Ionospheric electron density and temperature profiles using ionosonde-like data and machine learning. *Plasma*, *8*(2), 24. https://doi.org/10.3390/plasma8020024

Dubinin, E., Fraenz, M., Zhang, T., Woch, J., & Wei, Y. (2014). Magnetic fields in the Venus ionosphere: Dependence on the IMF direction—Venus express observations. *Journal of Geophysical Research: Space Physics*, *119*(9), 7587–7600. https://doi.org/10.1002/2014ja020195

Fowler, C., Andersson, L., Shaver, S., Thayer, J., Huba, J., Lillis, R., et al. (2017). MAVEN observations of ionospheric irregularities at Mars. *Geophysical Research Letters*, *44*(21), 10–845. https://doi.org/10.1002/2017gl075189

Fried, B. D., & Conte, S. D. (2015). *The plasma dispersion function: The Hilbert transform of the Gaussian*. Academic Press.

Gurevich, A., & Budden, K. (1980). Book-Review-Nonlinear phoenomena in the ionosphere. *The Journal of the British Astronomical Association*, *90*, 293.

Hoang, S. (1972). Admittance measurements of a 36-m dipole antenna in the topside ionosphere. *Planetary and Space Science*, *20*(8), 1185–1204. https://doi.org/10.1016/0032-0633(72)90007-4

Hoang, S., Steinberg, J. L., Epstein, G., Tilloles, P., Fainberg, J., & Stone, R. (1980). The low-frequency continuum as observed in the solar wind from ISEE 3: Thermal electrostatic noise. *Journal of Geophysical Research*, *85*(A7), 3419–3430. https://doi.org/10.1029/ja085ia07p03419

Hsu, C. T., Matsuo, T., Kershaw, H., Dietrich, N., Smith, M., Anderson, J., et al. (2024). A community ionosphere-thermosphere observing system simulation experiment (OSSE) tool: Geospace dynamics constellation example. *Earth and Space Science*, *11*(7), e2024EA003684. https://doi.org/10.1029/2024ea003684

Issautier, K., Meyer-Vernet, N., Moncuquet, M., & Hoang, S. (1996). A novel method to measure the solar wind speed. *Geophysical Research Letters*, *23*(13), 1649–1652. https://doi.org/10.1029/96gl01070

Issautier, K., Meyer-Vernet, N., Moncuquet, M., & Hoang, S. (1999). High-speed solar wind from Ulysses measurements and comparison with exospheric models. In *AIP Conference Proceedings* (Vol. 471(1), pp. 581–584). American Institute of Physics. https://doi.org/10.1063/1.58699

Jorge, R., Ricci, P., Brunner, S., Gamba, S., Konovets, V., Loureiro, N., et al. (2019). Linear theory of electron-plasma waves at arbitrary collisionality. *Journal of Plasma Physics*, *85*(2), 905850211. https://doi.org/10.1017/s0022377819000266

Kelley, M. C. (2009). *The Earth's ionosphere: Plasma physics and electrodynamics*. Academic Press.

Le Chat, G., Issautier, K., Meyer-Vernet, N., & Hoang, S. (2011). Large-scale variation of solar wind electron properties from quasi-thermal noise spectroscopy: Ulysses measurements. *Solar Physics*, *271*(1–2), 141–148. https://doi.org/10.1007/s11207-011-9797-3

Le Chat, G., Issautier, K., Meyer-Vernet, N., Zouganelis, I., Moncuquet, M., Hoang, S., et al. (2010). Quasi-thermal noise spectroscopy: Preliminary comparison between kappa and sum of two Maxwellian distributions. In *Paper presented at AIP Conference Proceedings* (Vol. 1216, pp. 316–319). American Institute of Physics. https://doi.org/10.1063/1.3395864

Liu, M. (2022). Large-scale solar wind properties by Parker Solar Probe and shock-foreshock interaction near the Earth. *Université Paris sciences et lettres*.

Liu, M., Issautier, K., Meyer-Vernet, N., Moncuquet, M., Maksimovic, M., Halekas, J., et al. (2021). Solar wind energy flux observations in the inner heliosphere: First results from Parker solar Probe. *arXiv preprint arXiv:2101.03121*, *650*, A14. https://doi.org/10.1051/0004-6361/202039615

Liu, M., Issautier, K., Moncuquet, M., Meyer-Vernet, N., Maksimovic, M., Huang, J., et al. (2023). Total electron temperature derived from quasi-thermal noise spectroscopy in the pristine solar wind from Parker Solar Probe observations. *Astronomy & Astrophysics*, *674*, A49. https://doi.org/10.1051/0004-6361/202245450

Luhmann, J., & Cravens, T. (1991). Magnetic fields in the ionosphere of Venus. *Space Science Reviews*, *55*(1), 201–274. https://doi.org/10.1007/bf00177138

Maj, R., & Cairns, I. H. (2017). Quasi-thermal noise and shot noise spectroscopy on a CubeSat in Earth's ionosphere. *Journal of Geophysical Research: Space Physics*, *122*(3), 3538–3552. https://doi.org/10.1002/2016ja023832

Maksimovic, M., Bale, S., Berčič, L., Bonnell, J., Case, A., de Wit, T. D., et al. (2020). Anticorrelation between the bulk speed and the electron temperature in the pristine solar wind: First results from the Parker solar probe and comparison with Helios. *The Astrophysical Journal - Supplement Series*, *246*(2), 62. https://doi.org/10.3847/1538-4365/ab61fc

Maksimovic, M., Bougeret, J. L., Perche, C., Steinberg, J., Lazarus, A., Vinas, A., & Fitzenreiter, R. (1998). Solar wind density intercomparisons on the WIND spacecraft using WAVES and SWE experiments. *Geophysical Research Letters*, *25*(8), 1265–1268. https://doi.org/10.1029/98gl00843

Martinović, M. (2016). *A study of quasi-thermal noise and shot noise in space plasmas*. Универзитет у Београду.

Martinović, M., Zaslavsky, A., Maksimović, M., & Šegan, S. (2017). Electrostatic thermal noise in a weakly ionized collisional plasma. *Radio Science*, *52*(1), 70–77. https://doi.org/10.1002/2016rs006189

Martinović, M. M., Đorđević, A. R., Klein, K. G., Maksimović, M., Issautier, K., Liu, M., et al. (2022). Plasma parameters from quasi-thermal noise observed by Parker solar probe: A new model for the antenna response. *Journal of Geophysical Research: Space Physics*, *127*(4), e2021JA030182. https://doi.org/10.1029/2021ja030182

Martinović, M. M., Klein, K. G., Gramze, S. R., Jain, H., Maksimović, M., Zaslavsky, A., et al. (2020). Solar wind electron parameters determination on Wind spacecraft using quasi-thermal noise spectroscopy. *Journal of Geophysical Research: Space Physics*, *125*(8), e2020JA028113. https://doi.org/10.1029/2020ja028113

Meyer, P., & Vernet, N. (1974). Impedance of a short antenna in a warm magnetoplasma. *Radio Science*, *9*(3), 409–416. https://doi.org/10.1029/rs009i003p00409

Meyer, P., & Vernet, N. (1975). The impedance of a dipole antenna in the ionosphere: 2. Comparison with theory. *Radio Science*, *10*(5), 529–536. https://doi.org/10.1029/rs010i005p00529

Meyer-Vernet, N. (1978). Impedance of a short antenna in a warm magnetoplasma: Experiment and comparison with theory. *Radio Science*, *13*(6), 1059–1068. https://doi.org/10.1029/rs013i006p01059

Meyer-Vernet, N. (1979). On natural noises detected by antennas in plasmas. *Journal of Geophysical Research*, *84*(A9), 5373–5377. https://doi.org/10.1029/ja084ia09p05373

Meyer-Vernet, N., Hoang, S., & Moncuquet, M. (1993). Bernstein waves in the Io plasma torus: A novel kind of electron temperature sensor. *Journal of Geophysical Research*, *98*(A12), 21163–21176. https://doi.org/10.1029/93ja02587

Meyer-Vernet, N., Issautier, K., & Moncuquet, M. (2017). Quasi-thermal noise spectroscopy: The art and the practice. *Journal of Geophysical Research: Space Physics*, *122*(8), 7925–7945. https://doi.org/10.1002/2017ja024449

Meyer-Vernet, N., & Perche, C. (1989). Tool kit for antennae and thermal noise near the plasma frequency. *Journal of Geophysical Research*, *94*(A3), 2405–2415. https://doi.org/10.1029/ja094ia03p02405

Miller, K. L., Knudsen, W. C., Spenner, K., Whitten, R. C., & Novak, V. (1980). Solar zenith angle dependence of ionospheric ion and electron temperatures and density on Venus. *Journal of Geophysical Research*, *85*(A13), 7759–7764. https://doi.org/10.1029/ja085ia13p07759

Moncuquet, M., Lecacheux, A., Meyer-Vernet, N., Cecconi, B., & Kurth, W. S. (2005). Quasi thermal noise spectroscopy in the inner magnetosphere of Saturn with Cassini/RPWS: Electron temperatures and density. *Geophysical Research Letters*, *32*(20). https://doi.org/10.1029/2005gl022508

Moncuquet, M., Meyer-Vernet, N., & Hoang, S. (1995). Dispersion of electrostatic waves in the Io plasma torus and derived electron temperature. *Journal of Geophysical Research*, *100*(A11), 21697–21708. https://doi.org/10.1029/95ja02299

Pandey, B., & Vladimirov, S. (2018). Dust modification of the plasma conductivity in the Earth's mesosphere. *Journal of Atmospheric and Solar-Terrestrial Physics*, *175*, 24–30. https://doi.org/10.1016/j.jastp.2018.05.003

Peter, K., Sánchez-Cano, B., Němec, F., González-Galindo, F., Kopf, A. J., Lester, M., et al. (2024). The ionosphere of Mars after 20 years of Mars Express contributions. *Space Science Reviews*, *220*(4), 41. https://doi.org/10.1007/s11214-024-01078-x

Rowland, D. E., Garcia-Sage, K., Kepko, L., Bishop, R. L., Deng, Y., Thayer, J. P., et al. (2022). The Geospace Dynamics Constellation (GDC) mission: NASA's next living with a Star mission to explore the Ionosphere/Thermosphere. In *Paper presented at AGU fall meeting abstracts* (Vol. 2022, pp. SA25C–1927).

Russell, C., Leinweber, H., Hart, R., Wei, H., Strangeway, R., & Zhang, T. (2013). Venus Express observations of ULF and ELF waves in the Venus ionosphere: Wave properties and sources. *Icarus*, *226*(2), 1527–1537. https://doi.org/10.1016/j.icarus.2013.08.019

Russell, C., & Vaisberg, O. (1983). The interaction of the solar wind with Venus. In *Venus* (pp. 873–940).

Sarkar, S., Atul, J. K., Laishram, M., Zou, D. D., Gulati, I., Singh, M. K., & Chattopadhyay, P. K. (2025). Parallel propagation effects on the dust acoustic drift instability in the equatorial electrojet. *Advances in Space Research*, *75*(6), 4795–4812. https://doi.org/10.1016/j.asr.2024.12.057

Shinagawa, H. (1996). A two-dimensional model of the Venus ionosphere: 2. Magnetized ionosphere. *Journal of Geophysical Research*, *101*(A12), 26921–26930. https://doi.org/10.1029/96ja01362

Spencer, E., Patra, S., Andriyas, T., Swenson, C., Ward, J., & Barjatya, A. (2008). Electron density and electron neutral collision frequency in the ionosphere using plasma impedance probe measurements. *Journal of Geophysical Research: Space Physics*, *113*(A9). https://doi.org/10.1029/2007ja013004

Tannous, S. M., Bonnell, J. W., Pulupa, M., & Bale, S. D. (2024). Electron temperatures in the Venusian ionosphere from Parker Solar Probe using quasi-thermal noise spectroscopy. *Geophysical Research Letters*, *51*(20), e2024GL110105. https://doi.org/10.1029/2024gl110105

Withers, P., Mendillo, M., Hinson, D. P., & Cahoy, K. (2008). Physical characteristics and occurrence rates of meteoric plasma layers detected in the Martian ionosphere by the Mars Global Surveyor Radio Science Experiment. *Journal of Geophysical Research: Space Physics*, *113*(A12). https://doi.org/10.1029/2008ja013636

Yoon, P. H., Kim, S., Hwang, J., & Shin, D. K. (2017). Upper hybrid waves and energetic electrons in the radiation belt. *Journal of Geophysical Research: Space Physics*, *122*(5), 5365–5376. https://doi.org/10.1002/2016ja023321

Zabotin, N. A., Bronin, A. G., Chugunov, Y. V., & Mareev, E. A. (2001). Analytical approach to calculate quasi-thermal noise spectrum in irregular plasma. *Astrophysics and Space Science*, *277*(1), 319–322. https://doi.org/10.1007/978-94-010-0904-1_41

Zheng, X., Martinović, M. M., Klein, K. G., Pierrard, V., Liu, M., Xue, X., et al. (2025). Quasithermal noise in magnetized plasma: Theory and simulations. *The Astrophysical Journal*, *985*(1), 114. https://doi.org/10.3847/1538-4357/add00f

Zheng, X., Martinović, M. M., Pierrard, V., Klein, K. G., Liu, M., Abraham, J. B., et al. (2024). Radial evolution of Non-Maxwellian electron populations derived from quasi-thermal noise spectroscopy: Parker solar probe observations. *The Astrophysical Journal*, *977*(1), 39. https://doi.org/10.3847/1538-4357/ad7d05